

A Continuum, $\mathcal{O}(N)$ Monte-Carlo algorithm for charged particles

Jörg Rottler* and A. C. Maggs†

Laboratoire de Physico-Chimie Théorique, UMR CNRS-ESPCI 7083, 10 rue Vauquelin, F-75231 Paris Cedex 05, France

(Dated: November 12, 2018)

We introduce a Monte-Carlo algorithm for the simulation of charged particles moving in the continuum. Electrostatic interactions are not instantaneous as in conventional approaches, but are mediated by a constrained, diffusing electric field on an interpolating lattice. We discuss the theoretical justifications of the algorithm and show that it efficiently equilibrates model polyelectrolytes and polar fluids. In order to reduce lattice artifacts that arise from the interpolation of charges to the grid we implement a local, dynamic subtraction algorithm. This dynamic scheme is completely general and can also be used with other Coulomb codes, such as multigrid based methods.

PACS numbers: 87.10.+e, 87.15.Aa, 41.20.Cv

I. INTRODUCTION

Simulating charged condensed matter systems is demanding due to the long range nature of the Coulomb interaction^{1,2}. The direct evaluation of the Coulomb sum for N particles, $U_c = \sum_{i<j} e_i e_j / 4\pi\epsilon_0 r_{ij}$, requires computation of the separations r_{ij} between all pairs of particles, which implies $\mathcal{O}(N^2)$ operations are needed per sweep or time step. Conventional fast algorithms including the classic Ewald sum³, particle mesh Ewald approaches^{4,5}, and fast multipole algorithms⁶ suffer from either poor scaling with system size, high coding complexity or inefficiency in multiprocessor environments. Although multigrid methods⁷ appear to be a promising candidate for fast parallelized molecular dynamics simulations, these techniques are less efficient for Monte-Carlo simulations, where the total energy of the system must be recalculated after *every* particle move.

It is surprising that the Coulomb interaction poses such tremendous difficulty; after all the underlying Maxwell equations are *local*. The above methods, however, do not solve Maxwell's equations, but rather search for the electrostatic potential $\phi_p(\mathbf{r})$, from which the electric field $\mathbf{E}(\mathbf{r})$ is deduced. We shall show in this article that this full relaxation of the electric field to the solution of the Poisson equation is not necessary in the context of statistical mechanics, where one is interested in configurational averages. This allows us to construct a nonstandard approach that is *local* and substantially more efficient than methods involving potential theory.

Recently, a lattice Monte-Carlo algorithm was introduced in which the time needed for a single sweep scales as only $\mathcal{O}(N)$. This algorithm employs the electric field, \mathbf{E} , rather than the scalar potential as the true degree of freedom^{8,9}. For a charge density $\rho(\mathbf{r}) = \sum_i e_i \delta(\mathbf{r} - \mathbf{r}_i)$, Gauss' law, $\epsilon_0 \text{div } \mathbf{E}(\mathbf{r}) - \rho(\mathbf{r}) = 0$, is imposed as an exact dynamical constraint on the field configurations. The algorithm correctly reproduced the static properties of a charged lattice gas and equilibrated the system with a $\mathcal{O}(1)$ overhead when compared to the time needed to simulate a neutral system¹⁰. This high efficiency results from purely local updates of particles and fields using the standard Metropolis Monte-Carlo rule; there is no global calculation of the potential.

In the present article, we generalize this algorithm to off-lattice Monte-Carlo, so that the particles move in the contin-

uum. Such a generalization is necessary for any realistic modeling of charged systems, such as polyelectrolytes, biopolymers and polar solvents. We begin with a complete description of the algorithm in Section II and continue with tests of the static and dynamic behavior in Section III. In particular, we demonstrate numerically that the slowest relaxation time in the charged system is dominated by diffusion of the density degrees of freedom, in a manner which is very similar to a neutral system with short range interactions. The following Section IV discusses the elimination of lattice artifacts that arise from the interpolation of charges to a grid via dynamic subtraction. Although demonstrated in the context of our auxiliary field Monte-Carlo algorithm, this dynamic subtraction can also be used with more conventional Coulomb algorithms such as multigrid.

II. COULOMB INTERACTIONS FROM AUXILIARY FIELDS

A. Constrained energy functional

The starting point for our derivation of a local Coulomb algorithm is a formulation of electrostatics in terms of a constrained energy functional based on a vector field $\mathbf{E}(\mathbf{r})$ ¹¹,

$$\mathcal{F}[\mathbf{E}] = \int \left[\frac{\epsilon_0 \mathbf{E}(\mathbf{r})^2}{2} - \phi(\mathbf{r})(\epsilon_0 \text{div } \mathbf{E}(\mathbf{r}) - \rho(\mathbf{r})) \right] d^3r. \quad (1)$$

In this functional Gauss' law is imposed with the Lagrange multiplier ϕ and constrains the longitudinal component of the electric field; $\phi(\mathbf{r})$ can be identified with the scalar potential ϕ_p . Minimization of the functional with respect to \mathbf{E} leads immediately to the familiar equations of electrostatics,

$$\mathbf{E} = -\nabla\phi_p \quad (2)$$

$$\nabla^2\phi_p = -\rho/\epsilon_0. \quad (3)$$

All conventional Coulomb algorithms are essentially concerned with finding solutions to Eqs. (2,3). After inserting Eqs. (2,3) into Eq. (1), we obtain the electrostatic energy $U_c = \frac{\epsilon_0}{2} \int (\nabla\phi_p)^2 d^3r$ as a minimum of the constrained functional. Note that a scalar functional based only on the potential

ϕ cannot be used, it leads to the wrong sign in the Coulomb interaction (see Ref. 10 for a discussion of this point).

The crucial point of our algorithm is now not to minimize the constrained energy functional Eq. (1), but rather to maintain the electric field at finite temperature. For $T > 0$, we have

$$\mathbf{E} = -\nabla\phi_p + \mathbf{E}_{tr}, \quad (4)$$

where $\mathbf{E}_{tr} = \text{curl } \mathbf{Q}$ is an arbitrary rotational vector field. The total field \mathbf{E} still satisfies Gauss' law, but the energy U is no longer equal to U_c , but rather $U = \frac{\epsilon_0}{2} \int \{(\nabla\phi_p)^2 + \mathbf{E}_{tr}^2\} d^3r$. We now show that an integration over these auxiliary transverse (rotational) degrees of freedom of the electric field nevertheless lead to electrostatic interactions.

To this end, let us consider the partial partition function for charged particles and a fluctuating electric field that is constrained by Gauss' law,

$$\mathcal{Z}(\{\mathbf{r}_i\}) = \int \mathcal{D}\mathbf{E} \prod_{\mathbf{r}} \delta(\text{div}\mathbf{E} - \rho(\{\mathbf{r}_i\})/\epsilon_0) e^{-\int d^3r' \epsilon_0 \mathbf{E}^2/2k_B T}. \quad (5)$$

Note that the integration is only performed over field configurations and not particle positions. We evaluate the integral by changing variables, $\mathbf{E}_{tr} = \mathbf{E} + \nabla\phi_p$,

$$\begin{aligned} \mathcal{Z}(\{\mathbf{r}_i\}) &= \int \mathcal{D}\mathbf{E}_{tr} \prod_{\mathbf{r}} \delta(\text{div}\mathbf{E}_{tr}) e^{-\int d^3r' \epsilon_0 (\mathbf{E}_{tr} - \nabla\phi_p)^2/2k_B T} \\ &= e^{-\int d^3r' \epsilon_0 (\nabla\phi_p)^2/2k_B T} \\ &\times \int \mathcal{D}\mathbf{E}_{tr} \prod_{\mathbf{r}} \delta(\text{div}\mathbf{E}_{tr}) e^{-\int d^3r' \epsilon_0 \mathbf{E}_{tr}^2/2k_B T} \\ &= \mathcal{Z}_{Coulomb}(\{\mathbf{r}_i\}) \times \text{const.} \end{aligned} \quad (6)$$

The cross term in the energy, $\int \mathbf{E}_{tr} \nabla\phi_p d^3r$, vanishes for periodic or constant potential boundary conditions, as can be seen by integration by parts. Eq. (6) shows that an integration over the transverse modes merely multiplies the coulombic partition function $\mathcal{Z}_{Coulomb}$ by a constant. Since this multiplication does not change the relative statistical weight of configurations, it can be ignored.

This result allows us to maintain the total electric field at finite temperature rather than quenching it to zero as when solving Poisson's equation. As long as the constraint of Coulomb's law is strictly maintained, an integration over all possible transverse field components will generate an effective Coulomb interaction between the particles. As illustrated below, this integration involves only local operations and requires no global optimization. Although this may sound unusual, it is actually a very natural way of calculating the interactions: we shall see below that the resulting dynamics has a local conservation law exactly as occurs in Maxwell's equations.

B. Algorithm

Our Monte-Carlo algorithm evaluates the partition function for a Coulomb system using the Metropolis criterion together

with the energy functional Eq. (1). The algorithm consists of two Monte-Carlo moves that

- integrate over the particle positions by displacing the charged particles, but maintain a field configuration that *always* satisfies Gauss' law;
- integrate over the transverse components of the electric field \mathbf{E}_{tr} to evaluate the configurational integral Eq. (6).

We shall now describe the implementation of the algorithm for the off-lattice case. A similar description of the algorithm for lattice simulations has already been given in Ref. 10. The reader who is only interested in the results of the algorithm may jump directly to Section III.

1. Discretization

Particles with charge $e_i = \pm 1$ move continuously in a cubic, periodic simulation cell of volume L^3 . The electric field \mathbf{E} is discretized onto a cubic grid of mesh size a , and the Cartesian components of \mathbf{E} are associated with the $3L^3/a^3$ links of the lattice. A natural unit of temperature or energy is $T^* \equiv e^2/4\pi\epsilon_0 k_B a$. In these units, the Bjerrum length is $l_b = aT^*/T$. A typical value in water at room temperature is $l_b \sim 7\text{\AA}$ for monovalent ions. Charges are interpolated onto the L^3/a^3 nodes of the lattice. Various choices are possible for the interpolation scheme: we desire a reasonably smooth interpolation and choose a 3rd order scheme using B-splines^{7,12}. In each Cartesian direction, the charge is distributed onto the 3 mesh points closest to the particle. Explicitly, the one-dimensional weights are

$$\begin{aligned} W_-([x]) &= ([x] - 0.5)^2/2 \\ W_0([x]) &= 0.75 - [x]^2 \\ W_+([x]) &= ([x] + 0.5)^2/2, \end{aligned} \quad (7)$$

where $[x]$ denotes the distance between the particle and the nearest lattice point in units of the lattice spacing. The three-dimensional weights are constructed by multiplying the three one-dimensional weights. Our method is not tied to a particular assignment scheme; higher or lower order schemes can be employed as long as they conserve charge exactly.

2. Particle motion and Hamiltonian paths

The simulation begins with a field configuration that satisfies the discretized, integral version of Gauss' law,

$$a^2 \sum_j E_{i,j} = e_i/\epsilon_0 \quad (8)$$

In this expression $E_{i,j} = -E_{j,i}$ denotes a field component leaving site i towards site j , and the sum is performed over all links connecting to site i ; it corresponds to the total flux leaving site i . The success of the algorithm depends on maintaining the constraint at all times; the field configuration is

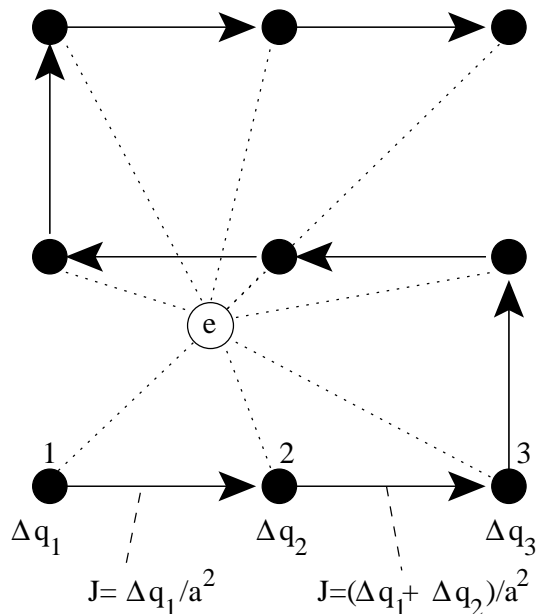


FIG. 1: Illustration of charge interpolation and the current update using a Hamiltonian path in two dimensions. A charge (open circle) interpolates onto the $3^2 = 9$ lattice sites (solid). The partial charges on these sites change by an amount Δq_i when the particle moves. The current J flows along the Hamiltonian path and terminates at the last site, since $\sum_i \Delta q_i = 0$.

updated each time a particle moves. For a lattice gas, such an update is easy to perform⁸: when a particle moves from site i to site j , one changes the field on the traversed link to $E_{i,j} \rightarrow E_{i,j} \mp e/(\epsilon_0 a^2)$ (the sign depends on the direction in which the particle moves). The resulting field configuration once again satisfies Eq. (8). The situation is more complicated in the off-lattice case; a single particle move changes the charges on $3^3 = 27$ nodes, more if the particle changes cells. One can choose among many update rules to realign the field configuration at all modified nodes (the system of equations is in general under-specified). This task can be accomplished with minimal effort using a path that traverses the modified region in such a way that it visits each site once. An example of such a path, which is often called a ‘‘Hamiltonian path’’, is shown for two dimensions in Fig. 1; the generalization to three dimensions is obvious. Only links along the path need be updated.

The field $E_{i,j}$ on a link that is part of the path is updated according to $E_{i,j} \rightarrow E_{i,j} \pm \sum'_s \Delta q_s / (\epsilon_0 a^2)$, where Δq_s denotes the change of the fractional charge on a node due to the particle motion. The primed summation extends over all sites that were previously visited by the path to reach site i , and the sign depends on the direction of the path. This update is efficiently performed during a single ‘‘walk’’ along the path. In a continuum description, the current that flows due to the motion of the particles produces a change in the electric field,

$$\frac{\partial \mathbf{E}}{\partial t} = -\mathbf{J}/\epsilon_0. \quad (9)$$

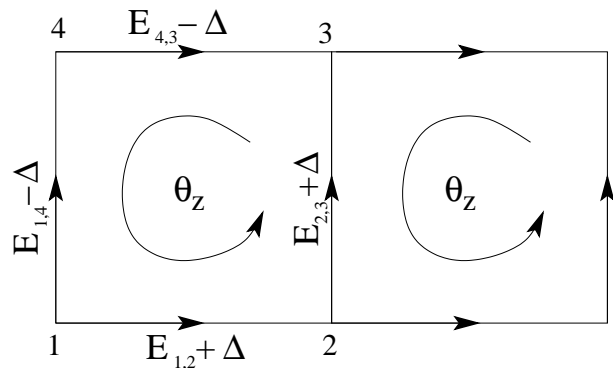


FIG. 2: Integration over the transverse degrees of freedom. The four link fields forming a plaquette in the xy -plane are modified by $\pm\Delta$ in such a way that the total field changes by a pure rotation ($\text{curl } \mathbf{E})_z = 4\Delta$. Δ is chosen from a uniform distribution. We associate an angular variable Θ_z with the plaquette so that $\delta \mathbf{E} = \text{curl } \delta \Theta$.

Note that though the path changes direction several times during the update, the resulting currents are essentially parallel. We always construct the Hamiltonian path in a manner which is symmetric between the new and old interpolation sites. Because of this our procedure is time reversible and the algorithm respects detailed balance. To simplify the implementation of the algorithm we always displace particles parallel to the links of the mesh with a step size uniformly distributed between 0 and a .

3. Integration over the transverse field

Field updates as described in the previous paragraph change not only the longitudinal component of the electric field, but simultaneously affect the transverse field. The particle motion thus already performs a partial integration over the transverse modes. A complete evaluation of the configurational integral Eq. (6) often requires a second type of Monte-Carlo move that changes just the transverse degrees of freedom of \mathbf{E} without moving a particle nor violating the constraint Eq. (8). This is done by grouping the links that form a faces of the grid into $3L^3$ plaquettes. We randomly choose a plaquette and increment the field on two of the links by an increment Δ while decreasing it on the other two; we only modify the total field configuration by a pure rotation (see Fig. 2). We describe the resulting dynamics by associating an angular variable θ_k with a plaquette in the $\{i, j\}$ -plane. As one can see by inspection of Fig. 2, changes in the electric field are related to the curl of the changes of the plaquette variable θ_k . Combining this with Eq. (9), the evolution of the electric field obeys the equation

$$\frac{\partial \mathbf{E}}{\partial t} = -\mathbf{J}/\epsilon_0 + \text{curl } \frac{\partial \vec{\theta}}{\partial t}. \quad (10)$$

Changes in \mathbf{E} also couple back to the circulatory degrees of freedom, one can show⁹ that $\text{curl } \mathbf{E}$ acts like a torque on $\vec{\theta}$, i.e.

$$\xi \frac{\partial \vec{\theta}}{\partial t} = -\epsilon_0 \text{curl } \mathbf{E} + \vec{\eta}, \quad (11)$$

where we have introduced a relaxation time scale ξ which is determined by the Monte-Carlo moves; $\vec{\eta}$ is a Brownian noise.

The dynamics of Eqs. (10,11) is closely related to the Maxwell equations¹¹. After identifying $\partial \vec{\theta} / \partial t$ with the magnetic field \mathbf{B} / μ_0 , we recover Ampere's law in Eq. (10). If we perform the same replacement in Eq. (11), we recognize its closeness to another Maxwell equation, Faraday's law. However, the usual $\partial \mathbf{B} / \partial t$ has been replaced by just \mathbf{B} ; a time derivative has been lost. By combining the two equations one finds⁹ that the electric field obeys a diffusion equation

$$\frac{\partial \mathbf{E}}{\partial t} = (\epsilon_0 \nabla^2 \mathbf{E} - \nabla \rho) / \xi - \mathbf{J} / \epsilon_0 + \text{curl } \vec{\eta}. \quad (12)$$

Since in Monte-Carlo we are interested in distributions rather than dynamics we are free to modify the underlying dynamics. Gauss' law is imposed as an initial condition and locally conserved both in Maxwell's equations and in our algorithm, as can be seen by taking the divergence of Eq. (12). The conservation of Gauss' law in our algorithm and in Maxwell's equation is the origin of Coulomb's law.

C. Boundary Conditions

Traditional treatments of the Coulomb interaction in periodic systems lead to a residual dependence on the dielectric constant ϵ' of a surrounding medium^{13,14}. For a standard Ewald summation, the short-range expansion of the pair potential between two point charges of opposite sign separated by r is¹⁵

$$V(r) = \frac{-e^2}{4\pi\epsilon_0 r} - \frac{e^2 r^2}{3\epsilon_0 L^3} \left(\frac{\epsilon' - 1}{2\epsilon' + 1} \right) + \mathcal{O}(r^4) \quad (13)$$

The present algorithm imposes a different choice that we denote "Maxwell" boundary conditions, since they are the same as those generated by the full Maxwell equations. We show in the appendix that

$$V(r) = \begin{cases} \frac{-e^2}{4\pi\epsilon_0 r} + \frac{e^2 r^2}{3\epsilon_0 L^3} + \mathcal{O}(r^4) & \text{for } l_b \gg L \\ \frac{-e^2}{4\pi\epsilon_0 r} - \frac{e^2 r^2}{6\epsilon_0 L^3} + \mathcal{O}(r^4) & \text{for } l_b \ll L \end{cases}. \quad (14)$$

There is again a quadratic correction to the bare $1/r$ interaction, which, surprisingly, depends on the temperature. A crossover occurs when the Bjerrum length l_b reaches the system size L . It is possible to remove the temperature dependence of the potential by introducing a third type of Monte-Carlo move that couples to the mean or $\mathbf{q} = 0$ component of the electric field $\vec{\mathbf{E}} = \frac{1}{L^3} \int d^3r \mathbf{E}(\mathbf{r})$. The potential then coincides with the conventional Ewald sum with "tinfoil" ($\epsilon' = \infty$) boundary conditions.

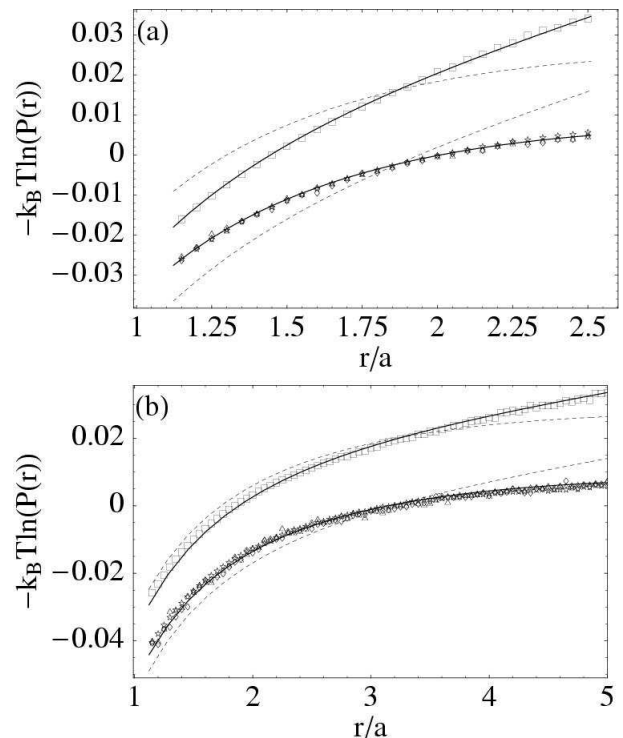


FIG. 3: Pair potentials obtained from the distribution $P(r)$ at distance r of a pair of charges for two system sizes (a) $L = 5a$ and (b) $L = 10a$ and two different temperatures $T_l = 0.065T^*$ (\square, \star) and $T_h = 1T^*$ (\triangle, \diamond). Solid lines Eq. (14), $V(r) = \text{const} - 1/4\pi r - b(T)r^2$, where the limiting values for the quadratic correction are $b(T_l) = -1/3\epsilon_0 L^3$ and $b(T_h) = 1/6\epsilon_0 L^3$ for Maxwell boundary conditions (\square, \triangle) (dashed lines show the curves in the opposite limit to demonstrate sensitivity). Addition of a third move leads to tinfoil boundary conditions (\star, \diamond), $b \equiv -1/3\epsilon_0 L^3$ for all T . All curves end at $r = 2^{1/6}a$, where the particles interact with the truncated Lennard-Jones potential.

III. RESULTS

A. Static quantities

1. Pair potential

We begin the analysis of the algorithm by verifying that the effective interaction between particles is in agreement with Eq. (14). We evaluated the pair potential by placing two particles of opposite charge in the simulation cell and measuring the distribution $P(r)$ of separations between the particles for different temperatures and system sizes. The negative logarithm of $P(r)$, which is proportional to the pair potential, is shown in Fig. 3 together with the curve Eq. (14). To include self-avoidance, a purely repulsive truncated Lennard-Jones potential of range a was added to the interaction. Overall, we find excellent agreement between Eq. (14) and the numerical curves. For Maxwell boundary conditions, the quadratic correction depends on temperature, and the two temperatures shown in Fig. 3 correspond to the limiting values of Eq. (14).

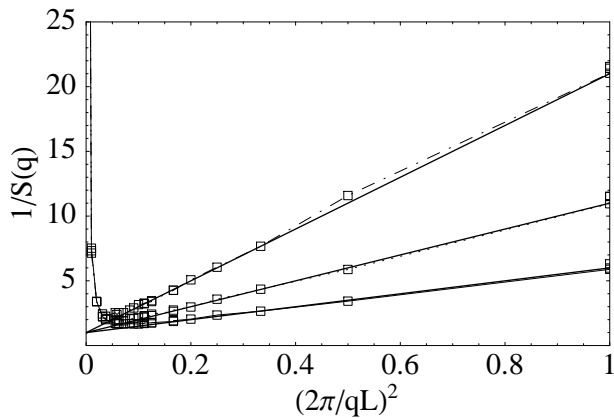


FIG. 4: Static charge-charge structure factor for a simple Coulomb gas at $T = 1.25T^*$ and three different densities $\rho = 0.05 a^{-3}$, $\rho = 0.1 a^{-3}$, and $\rho = 0.2 a^{-3}$. The slopes at large values of $1/q^2$ increase linearly with density as expected for Debye screening.

The Ewald convention with ‘tinfoil’ boundary conditions has also been simulated by performing additional integration over the mean field $\bar{\mathbf{E}}$. In this case, all curves collapse onto the $l_b \ll L$ Maxwell result for all temperatures. To reduce lattice artifacts at short distances, a dynamic subtraction (that will be discussed in a subsequent section) was employed for the curves of Fig. 3.

2. Screening

One of the characteristic features of systems containing mobile charges is the phenomenon of screening; the effective interactions decay exponentially with the inverse Debye screening length $\kappa^2 = ne^2/\epsilon_0 k_B T$, where n denotes the density of the charge carriers. At high enough temperatures the static charge-charge structure factor of a screened system has the form

$$S(q) = \frac{e^2 q^2}{\kappa^2 + q^2}. \quad (15)$$

In order to test whether our algorithm reproduces correctly this essential property of charged systems, we consider a globally neutral polyelectrolyte composed of positive and negative particles (together with a short ranged Lennard-Jones potential) and equilibrate it at the temperature $T = 1.25T^*$. We then measure the static structure factor

$$S(q) = \langle s(\mathbf{q})s(-\mathbf{q}) \rangle, \quad s(\mathbf{q}) = \frac{1}{\sqrt{N}} \sum_i e_i \exp(i\mathbf{r}_i \cdot \mathbf{q}) \quad (16)$$

and compare its form to Eq. (15) in Fig. 4 by plotting $1/S(q)$ as a function of $1/q^2$. As can be seen, the long wavelength data falls along a straight line, whose slope varies with particle density. The solid lines have slope $\kappa^2 L^2/4\pi^2$ and are in good agreement with the numerics.

B. Efficiency

Having shown that the algorithm behaves correctly, we now turn to a study of the dynamics. As already discussed in⁹, the Monte-Carlo update rules lead to a diffusive dynamics of the longitudinal and transverse fields, and we wish to explore how quickly our off-lattice algorithm equilibrates various modes of the system.

1. Dynamics of free charges

We investigate the dynamics of the simple Coulomb gas shown in Fig. 4 by studying the time decay of correlations in Fourier space. We measure the dynamical structure factors $S(\mathbf{q}, t) = \langle s(\mathbf{q}, t)s(-\mathbf{q}, 0) \rangle$ with $s(\mathbf{q}, t) = \frac{1}{\sqrt{N}} \sum_i e_i \exp(i\mathbf{q} \cdot \mathbf{r}_i(t))$, where the weights e_i are replaced by unity when measuring density correlations. We also examine correlations in the transverse electric field (that part of the field for which the discrete divergence, Eq. (8) is zero). The correlation functions for a single wavevector are shown in Fig. 5(a). All modes decay exponentially; time is measured in ‘particle sweeps’; in one time unit we attempt to update each particle once together with a variable number of plaquettes (see below).

By fitting the correlation functions to exponentials, we extract decay rates for selected modes and plot the resulting dispersion relations in Fig. 5(b). As can be seen, the density modes (\square) are diffusive at small wavevectors, $\omega \propto q^2$, but the longitudinal (\blacktriangle) and transverse (\diamond) modes of the electric field have a gap at $q = 0$, $\omega \propto \omega_0 + q^2$. This behavior can be compared to the continuum equations describing a gas of free charge carriers (see also ref. 9). The mean current is driven by the electric field and the charge density gradient,

$$\mathbf{J} = ne^2\alpha\mathbf{E} - D\nabla\rho. \quad (17)$$

n is the number density, D a diffusion coefficient that is related to the mobility α via the Einstein relation $D = k_B T\alpha$. We insert this relation into the diffusion equation (12) to study the dispersions of the longitudinal and transverse field components.

First, we take the curl of Eq. (12) and Fourier transform to find the relation

$$(i\omega + \epsilon_0 \mathbf{q}^2/\xi + ne^2\alpha/\epsilon_0)\hat{\mathbf{E}}_{tr} = 0. \quad (18)$$

As observed in Fig. 5(b), the transverse modes diffuse with a diffusion constant that is determined by ξ , a characteristic relaxation time scale related to the frequency of updates of the transverse field components. In the absence of charges, the relaxation time $\omega \rightarrow 0$ as $q \rightarrow 0$, but the presence of a charge density induces a gap $\omega_0 = Dne^2/k_B T = D\kappa^2$ in the spectrum. The origin of this gap is the screening of the interactions on a scale given by the inverse Debye screening length κ^2 .

For the longitudinal field components, we find that

$$(i\omega + D\mathbf{q}^2 + ne^2\alpha/\epsilon_0)\mathbf{q} \cdot \mathbf{E} = 0. \quad (19)$$

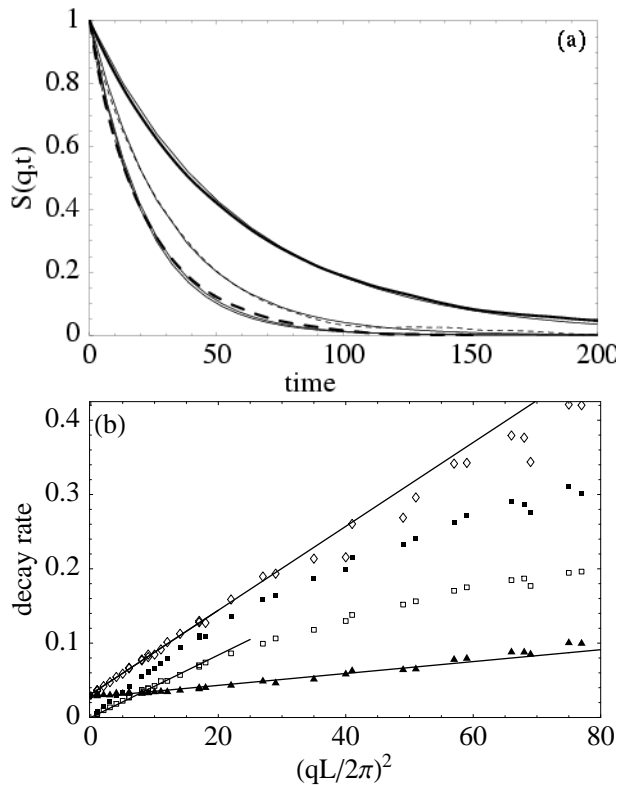


FIG. 5: (a) Relaxation of particle (thick solid line), charge (thin dashed line) and transverse field (thick dashed line) correlations as well as exponential fits. System size $L = 20a$, $\rho = 0.2a^{-3}$, $T = 1.25T^*$, mode (1,1,1). (b) Dispersion relations for particle (\square), charge (\blacktriangle) and transverse field (\diamond). Also shown is the density dispersion relation for a neutral system (\blacksquare) with otherwise identical parameters.

Again we find a gap in the spectrum with the same frequency ω_0 as for the transverse modes. We have also computed numerically the relaxation of the field correlations $\langle \mathbf{E}(t) \mathbf{E}(0) \rangle$ in real space, which corresponds to the $q = 0$ mode in Fig. 5(b). This frequency coincides with ω_0 .

Fig. 5 provides the basic demonstration of the efficiency of the algorithm. The slowest relaxation time of the system corresponds to particle diffusion and scales quadratically with system size; any meaningful statistical average must equilibrate the system over that timescale. The charge and transverse fluctuations relax much faster than the density fluctuations, and in Monte-Carlo one is free to tune the “diffusion constant” (the slope of the straight line) for the transverse field by adjusting the relative frequency of plaquette to particle updates. If we update the transverse field very often then we converge to the classic algorithms with instantaneous propagation of the electric field. However, even very rare transverse updates will still equilibrate the transverse field components.

For Fig. 5, we have chosen a high frequency of transverse mode updates, where we update typically 2/3 of all plaquettes in one particle sweep. Nevertheless, we estimated only about 15% CPU time is needed for this part of the simulation, all other time was consumed by the particle updates (essentially

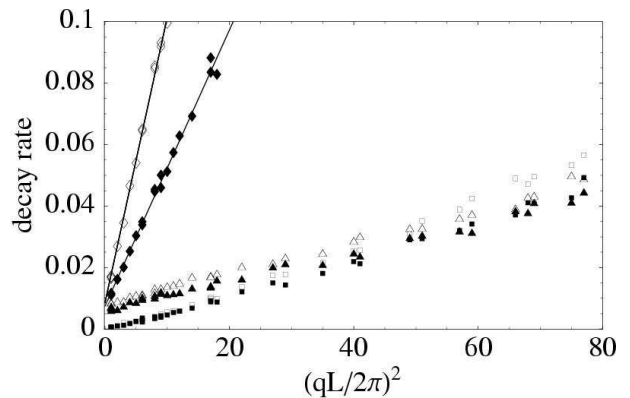


FIG. 6: Dispersion relations in a simulation with system size $L = 20a$, $\rho = 0.01a^{-3}$, $T = 0.125T^*$ for particles (\square), longitudinal (\triangle) and transverse fields (\diamond). For the solid symbols the transverse fields were updated less frequently (see text).

charge interpolation plus the Hamiltonian path). We dropped the frequency of plaquette updates by a factor of 10 and observed no change in the relaxation of the density and charge correlations. This result indicates that in a reasonably dense system, the particle motion alone is already performing a substantial part of the integration over the transverse modes. Our simple analytic theory predicts exactly this: even in the limit of slow propagation of the transverse field the longitudinal dynamics equilibrate.

As an additional illustration of the efficiency of the algorithm, we replaced the charged particles of Fig. 5(b) with neutral particles and repeated the simulation with otherwise identical parameters. The particle dispersion (\blacksquare) shows that the neutral particles diffuse about two times faster, since they are not slowed down by the electric field. We conclude that the price for simulating this dense charged system is an overhead of only about a factor of 2 in particle sweeps (though clearly in a neutral system one does not need charge interpolation which is relatively costly in cpu time).

It is clear that the algorithm exhibits strict $\mathcal{O}(N)$ scaling (at least away from critical points), since the work for moving a particle is purely local and consists essentially in the charge interpolation. One might object that the algorithm is surely inefficient at very low densities: the effort needed to update the plaquettes must become overwhelming. To characterize the speed of our algorithm in such an unfavorable situation, we contrast the high temperature, high density simulation of Fig. 5 with a simulation at a lower temperature $T = 0.125T^*$ and density $\rho = 0.01a^{-3}$ in Fig. 6. It is now necessary to perform more plaquette updates than before; most particles have condensed into pairs that move slowly and cannot easily integrate over the transverse field. For the open symbols in Fig. 6 we update each plaquette once per particle sweep and achieve a very high relaxation rate for the transverse field. The computational effort for the transverse updates is about 70% of the total runtime in this case. We dropped the frequency of transverse updates by a factor of two (filled symbols), but the longitudinal and transverse relaxation rates only dropped by about 10%.

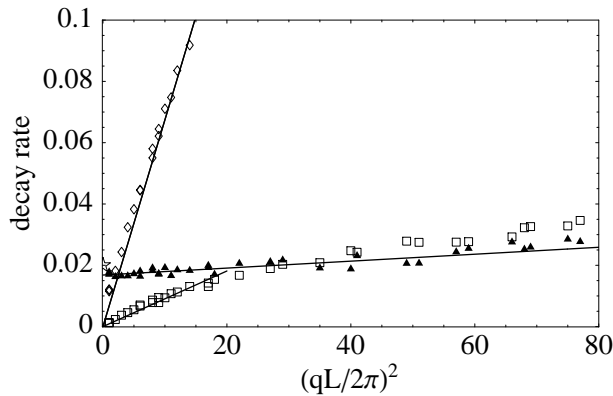


FIG. 7: Dispersion relations for particle (\square), charge (\blacktriangle) and transverse field (\diamond) for simple dipoles. System size $L = 20a$, $\rho = 0.2a^{-3}$, $T = 1.25T^*$, $k = 8\pi T^*$.

We should note that we are using a very simple Monte-Carlo procedure in this low density system, which chooses plaquettes randomly in the simulation cell. One can easily bias the choice of the plaquette to be in the neighborhood of a particle without violating detailed balance. Initial tests on our lattice implementation⁸ have shown substantial increase in efficiency at very low densities (volume fraction of 10^{-4}) with such a choice. We therefore anticipate that simple, local optimizations will greatly improve the performance of the algorithm for very dilute systems at low T , but leave a detailed exploration of this point to future work.

2. Dynamics of polar molecules

In the previous paragraph, we argued that relaxation of the simple Coulomb gas is aided by screening due to the gap in the relaxation spectrum. It is therefore interesting to ask how the algorithm performs on a non-screening system. To this end, we create polar molecules by coupling two particles with opposite charge with a harmonic spring of the form $V_b(r) = k(r - r_0)^2$. In Fig. 7, we show the dispersion relations for this polar system.

Comparing with Fig. 5, we observe that the spectrum for the transverse modes (\diamond) no longer has a gap, but rather extrapolates to zero at $q = 0$. However, the dispersion continues to be diffusive, and the transverse modes can be relaxed at any desired rate by varying the number of plaquette updates per sweep. The longitudinal (\blacktriangle) spectrum continues to exhibit a gap, but its magnitude is now determined by the spring stiffness governing the internal vibrations of the molecule. The efficiency of the algorithm is independent of the presence of screening, and the relaxation of the transverse modes is not impeded by the longitudinal field.

C. Numerical stability

Another appealing feature of the algorithm besides its simplicity is its numerical stability. Every update of the field on a

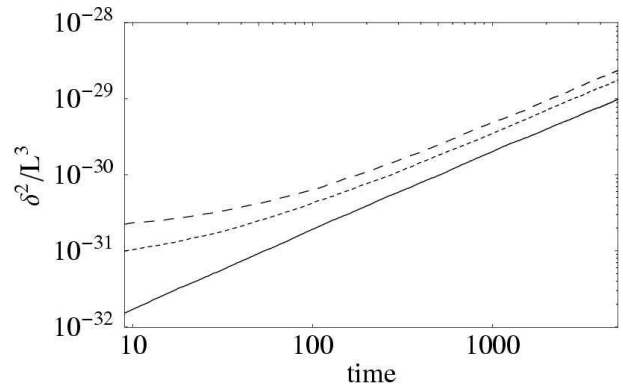


FIG. 8: Squared deviation from Gauss' law/site as a function of time in a simulation of size $L = 20a$, where the number of particles $N = 0$ (solid), $N = 800$ (dashed) and $N = 1600$ (long dashed).

link, be it through particle motion or plaquette updates, involves a numerical error of order the machine precision (typically $\mathcal{O}(10^{-16})$). Although this error is cumulative over time, it increases so slowly that the accuracy should remain acceptable even for the longest run times. To investigate the stability of our code, we averaged the deviation of the field configuration from Gauss's law Eq. (8), $\delta^2 = (a^2 \sum_j E_{i,j} - e_i/\epsilon_0)^2$ over the entire simulation cell and plot this quantity as a function of time in Fig. 8. Time was again measured in Monte-Carlo sweeps. We find a diffusive growth for the error/site, $\delta^2/L^3 = \text{const.} \times 10^{-32}t$. The constant is smallest for an empty system and increases slowly with the number of particles, but is always less than one. Since the equilibration time is of order $\mathcal{O}(L^2)$, even the largest systems equilibrate with acceptable errors.

IV. DYNAMIC SUBTRACTION OF LATTICE ARTEFACTS

Many conventional fast electrostatic methods (and the present algorithm) interpolate the point charges onto an electric grid in order to exploit the fast Fourier transform (FFT)¹⁷ or multigrid algorithms¹². Such an interpolation introduces a set of artefacts that have to be controlled: at short scales, the interaction between the charge clouds will in general differ from that of point charges; furthermore, the self energy \mathcal{U}_{self} of an interpolated charge distribution $\rho_{int}(\mathbf{r})$ becomes a function of its position with respect to the mesh. In general,

$$\begin{aligned} \mathcal{U}_{self} &= \frac{1}{2} \int d^3r d^3r' G(\mathbf{r} - \mathbf{r}') \rho_{int}(\mathbf{r}) \rho_{int}(\mathbf{r}') \\ &= \frac{1}{2} \int \frac{d^3q}{(2\pi)^3} \hat{G}(\mathbf{q}) S_{int}(\mathbf{q}) \end{aligned} \quad (20)$$

where $S_{int}(\mathbf{q})$ is the structure factor of the interpolation of the charge to the mesh. For the Coulomb interaction, the Green functions are $G_{coul}(r) \sim 1/r$ and $\hat{G}_{coul}(q) \sim 1/q^2$ in real and Fourier space, respectively, so that the integral diverges linearly for $q \rightarrow \infty$. This leads to a periodic potential which has an amplitude ΔU_s of order $\mathcal{O}(e^2/\epsilon_0 a)$ for mesh size a .

Use of a finer mesh leads to worse results with the simplest interpolation schemes. The periodic potential tends to “trap” the particles in the center of the grid cubes where the self-energy is lowest.

The conventional remedy to the situation consists simply in spreading out the charge over a wider range of sites, thereby reducing the self-energy artifacts. This is typically done with a convolution step that distributes the charges over several hundred sites using Gaussians¹² after interpolation to the lattice. These convolutions are easy to perform in Fourier space, but are complicated and time consuming in real space. They would also drastically reduce the speed of our algorithm, since the Hamiltonian path would have to visit many more sites in order to properly update the field configuration.

Here, we introduce a dynamic correction that leads to an effective convolution of the charge distribution with minimal computational overhead. For simplicity, we initially work in a continuum picture before discretizing and consider the unconstrained scalar functional

$$\mathcal{F}_Y[\psi] = \int \left[\frac{\epsilon_0}{2} [(\nabla\psi)^2 + \mu^2\psi^2] - \rho\psi \right] d^3r \quad (21)$$

Minimizing this functional with respect to the field ψ leads to the Yukawa equation

$$(\nabla^2 - \mu^2)\psi_Y = -\rho/\epsilon_0. \quad (22)$$

Substituting the solution ψ_Y into Eq. (21), we find a *negative* Yukawa Green function. The negative sign of the Green function is a feature of the scalar energy functional that we exploit here. By coupling the charge density ρ in our simulation to the scalar functional Eq. (21), we generate the partition function

$$\mathcal{Z}_Y(\mathbf{r}) = \int \mathcal{D}\psi e^{-\mathcal{F}_Y[\psi](\mathbf{r})/k_B T} \quad (23)$$

and the particles interact with the Yukawa potential

$$V_Y(r) = -\frac{e_1 e_2}{4\pi\epsilon_0 r} e^{-\mu r}. \quad (24)$$

The essence of our dynamic subtraction algorithm is to couple the charges *simultaneously* to the unconstrained functional Eq. (21) as well as the constrained vector functional, Eq. (1). The total partition function then reads

$$\mathcal{Z}(\mathbf{r}) = \mathcal{Z}_{Coulomb}(\mathbf{r}) \times \mathcal{Z}_Y(\mathbf{r}) \times \text{const.} \quad (25)$$

and implies an effective interaction between two charges e_1 and e_2 given by

$$V(r) = \frac{e_1 e_2}{4\pi\epsilon_0 r} (1 - e^{-\mu r}). \quad (26)$$

At large separations we find the Coulomb interaction; at small distances the potential has been regularized. The corresponding Green’s function for eq.(26) is the sum of the Green’s functions for Coulomb and Yukawa interaction,

$$\hat{G}(\mathbf{q}) = \frac{1}{\mathbf{q}^2} - \frac{1}{\mathbf{q}^2 + \mu^2} = \frac{\mu^2}{\mathbf{q}^2(\mathbf{q}^2 + \mu^2)} \quad (27)$$

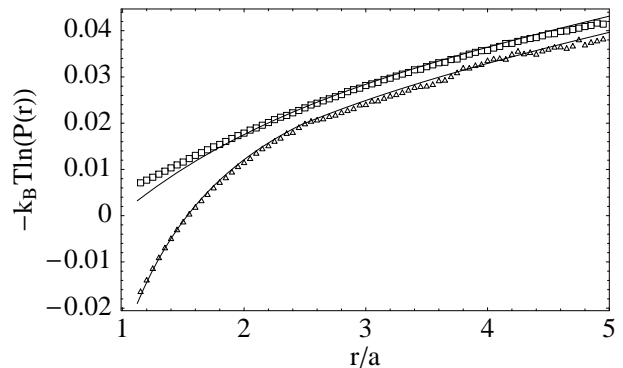


FIG. 9: Pair potential for combined Coulomb/Yukawa interaction at $T = 0.0625T^*$, $L = 10a$, $\mu = 0.75a^{-1}$. The top curve (□) shows the full combination in agreement with $V(r) = \text{const} - (1 - \exp[-\mu r])/4\pi\epsilon_0 r - r^2/3\epsilon_0 L^3$ (solid line). In the lower curve (△), the Yukawa interaction was removed for distances up to $r \leq 2.5a$. For the curves shown in Fig. 3 the Yukawa interaction was removed up to $L/2$.

By inserting eq. (27) into Eq. (20), we find that the self-energy is now finite for $a \rightarrow 0$. We can interpret the factor that multiplies the bare Coulomb Green function on the right of eq.(27) as a structure factor $S_{conv}(\mathbf{q}) = \mu^2/(q^2 + \mu^2)$ describing a convolution of the original charge density. In real space, this convolution function is

$$\int_{-\infty}^{\infty} \frac{d^3\mathbf{q}}{(2\pi)^3} S_{conv}(\mathbf{q})^{1/2} e^{-i\mathbf{q}\cdot\mathbf{r}} = \frac{\mu^2}{2\pi^2} \frac{K_1(\mu r)}{r}, \quad (28)$$

where K_1 is a modified Bessel function.

Use of the scheme Eq. (26) allows us to construct an efficient algorithm, since it requires only the introduction of a scalar field with Monte-Carlo moves and coupling to the charge density according to Eq. (21). The additional overhead of the dynamics of this supplementary field is small, since we reuse the same values of the interpolated charges for the vector and scalar fields. The run time complexity of the dynamic correction is independent of μ . Small values of μ give maximum smoothing, but also strongly alter the interaction at small distances. In general, one therefore wants to remove the Yukawa interaction on a scale of $1/\mu$ by adding $-V_Y(r)$ to the interaction. This can be conveniently done together with all the other short range (e. g. van der Waals) interactions of the system. The choice of μ therefore gives us a freely tunable tradeoff between precision and efficiency. This algorithm reminds us of early attempts at creating finite field theories in the 1940’s¹⁸ using different particles to cancel divergences in physical quantities. Here it is the ground state energies of two Gaussian field theories (but with scalar and vector symmetries) which have compensating divergences in the continuum limit, leading to a finite theory when they are combined.

We have implemented the above method in our off-lattice Monte-Carlo simulation to test its validity and efficiency. To this end, Monte-Carlo moves for the second auxiliary field ψ were introduced to generate the effective interaction Eq. (26). We first verified this interaction by extracting the pair potential from the distribution of separation $P(r)$ of a pair of

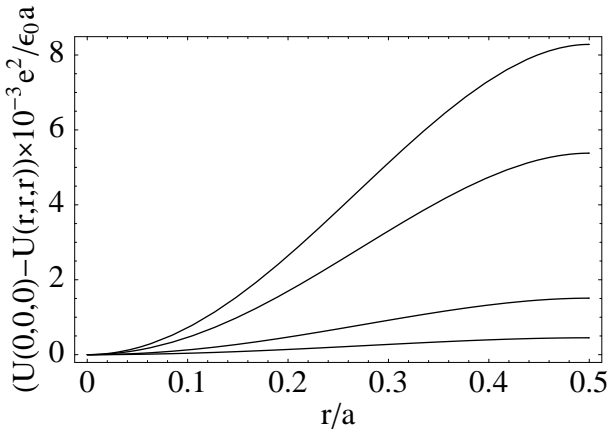


FIG. 10: Self energy along the diagonal of a grid cube from corner $(0, 0, 0)$ to center $(0.5, 0.5, 0.5)$ for the pure Coulomb interaction (lowest curve) and the combined Coulomb/Yukawa interaction for $\mu = 3a^{-1}$, $\mu = 1a^{-1}$, and $\mu = 0.5a^{-1}$ (highest curve). Charges were interpolated using B-splines, and the energies were calculated using the lattice Green function Eq. (29).

charges as in Sec. III A 1. The top curve in Fig. 9 shows the combined Yukawa and Coulomb interaction for a value of $\mu = 1$ in the low temperature limit of Maxwell boundary conditions. The Yukawa field was updated much more rarely than the transverse electric field since the massive field relaxes rapidly. The curve agrees well with the analytic expression $V(r) = \text{const} - (1 - \exp[-\mu r])/4\pi\epsilon_0 r - r^2/3\epsilon_0 L^3$ except at small distances where the interpolated charges overlap. The Yukawa potential can be subtracted Eq. (24) explicitly at short distances. The lower curve shows a case where this was done for $r < 2.5a$; the numerical points agree well with the Coulomb potential. Note that this correction at small scales should in fact not be necessary in realistic applications that use a grid size a that is much smaller than the LJ particle radii.

We now have to show that the imposition of an additional Yukawa interaction also reduces the self-energy artifacts. The most dramatic manifestation of these artifacts occurs through a trapping of particles in the cell center due to the (periodic) energy barrier $\Delta U_s = U_{\text{corner}} - U_{\text{center}}$, where U_{center} and U_{corner} are the self energies of a particle located at the center or corner of a grid cube. The self energy of a particle whose charge is interpolated onto the cubic grid with the B-spline interpolation Eq. (7) can be calculated using the lattice Green function for the Yukawa interaction,

$$G_\mu(\mathbf{r}) = \int \frac{d^3\mathbf{q}}{(2\pi)^3} \frac{e^{i\mathbf{q}\cdot\mathbf{r}}}{6 - 2\cos q_x - 2\cos q_y - 2\cos q_z + \mu^2} \quad (29)$$

We evaluated Eq. (29) numerically using Mathematica. Fig. 10 shows the self-energy along the diagonal of a grid cube for for the combined Coulomb/Yukawa interaction for several values of μ . The amplitude of this potential is largest for the pure Coulomb case and is drastically reduced when $\mu = 0.5a^{-1}$

In our Monte-Carlo simulations, ΔU_s has been extracted from the ratio of probabilities to find the particle in the center or corner, respectively. In Fig. 11, we show the effective

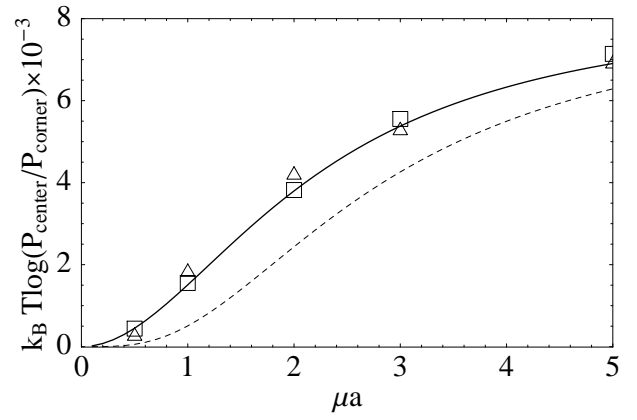


FIG. 11: Reduction of the self energy barrier leading to trapping of particles in cell centers. Numerical points correspond to temperatures $T = 0.0625T^*$ (\square) and $T = 0.125T^*$ (\triangle). The probabilities were measured by counting particles in cubic regions centered in center and corner of size $0.4^3 a^3 = 0.064a^3$. The lines show the expected reduction of the energy barrier based on a semi-analytic evaluation of the self-energy using the scheme Eq. (26) (solid line) and Eq. (31) (dashed line).

self-energy barriers obtained in this way as a function of μ . As expected from Fig. 10, the barrier drops rapidly with decreasing μ , and almost complete elimination is achieved at a value of $\mu = 0.5a^{-1}$. The solid line in Fig. 11 was obtained by computing the self energy difference of particles located in the center and corner of the grid cube as shown in Fig. 10. The numerical points agree well with this result.

From the numerical integration of Eq. (29), we find that the amplitude of the periodic energy barrier varies as $\Delta U_s(\mu) = 2 \times 10^{-3} (\mu a)^2 T^*$ for small μ . Even better smoothing should be possible if one uses a mixture of Green functions that decays even faster for large wavevectors than Eq. (27): Let us consider

$$\hat{G}(\mathbf{q}) = \frac{2\mu^4}{\mathbf{q}^2(\mathbf{q}^2 + \mu^2)(\mathbf{q}^2 + 2\mu^2)}, \quad (30)$$

The corresponding real space potential is

$$V(r) = \frac{e_1 e_2}{4\pi\epsilon_0 r} (1 - 2e^{-\mu r} + e^{-\sqrt{2}\mu r}), \quad (31)$$

which can be generated by coupling the charges to three fields, respectively a constrained vector, a scalar and an *unconstrained* vector. This unconstrained vector functional reads

$$\mathcal{F}_\mu[\mathbf{E}] = \int \left[\frac{\epsilon_0 \mathbf{E}(\mathbf{r})^2}{2} - \frac{(\epsilon_0 \text{div } \mathbf{E}(\mathbf{r}) - \rho(\mathbf{r}))^2}{2\mu^2} \right] d^3r. \quad (32)$$

which leads to a Yukawa Green function with a positive prefactor. The dashed line in Fig. 11 shows the energy barrier as a function of μ for this scheme. The inhomogeneity in the self energy is smaller than when using only the scalar Yukawa functional, and the barrier now varies as $\Delta U_s(\mu) = 1.5 \times 10^{-3} (\mu a)^4 T^*$ for small μ . Although we have not implemented this full scheme in our Monte-Carlo simulation, it

appears to be the strategy of choice when optimizing the algorithm for truly atomistic, high accuracy simulations. We note that the success of the method requires that both the vector and scalar functionals implement equivalent discretizations of the Laplacian operator. In our code this is the simplest 7-point difference scheme.

We would like to emphasize that the present strategy is general and can also be used in combination with other Coulomb algorithms. Methods relying on solutions of the Poisson equation could simulate an additional Yukawa equation and add the resulting potentials or forces. This seems to be rather attractive, since the charge spreading step amounts to a significant portion of the total computational effort in multigrid formulations⁷.

V. CONCLUSIONS

We have implemented a Monte-Carlo algorithm for charged particles moving in the continuum. Instead of minimizing the electrostatic energy, the algorithm uses particle moves in combination with constrained auxiliary field updates whose dynamics are inspired by the full Maxwell equations. Unlike in electrodynamics, however, the field propagates diffusively. We showed that the algorithm efficiently equilibrates charged systems such as electrolytes and polar fluids. It is most efficient at higher densities and temperatures, where the particle motion alone can perform a substantial part of the integration over the transverse modes of the electric field. Even at lower temperatures, the cost for the transverse integration remained acceptable.

We also introduced an approach to treat lattice artifacts that arise from the charge interpolation onto a grid. By introducing an additional negative Yukawa interaction, the periodic potential arising from the self-energy of the particles can be reduced to any desired accuracy. The scheme is completely general, and other Coulomb algorithms could also benefit from the method.

The principal advantages of the present approach are

- True $\mathcal{O}(N)$ scaling with the number of particles in the system. No such algorithm is available for Monte-Carlo simulations at present. Many problems involving electrostatics that could previously only be treated efficiently with molecular dynamics can now be treated with Monte-Carlo, which is often easier to program and faster due to larger time steps.
- Purely local computations are required to advance particle and field degrees of freedom, making the algorithm an ideal candidate for parallelization on large compute clusters or supercomputers.

In the present form, the algorithm can treat coarse-grained models of e. g. polyelectrolytes or membranes. It now has to pass more stringent tests with realistic model systems and truly atomistic simulations.

VI. ACKNOWLEDGMENTS

We thank R. Everaers and L. Levrel for very stimulating discussions of this work. JR thanks the CNRS for financial support through a ‘‘poste rouge’’ fellowship.

APPENDIX A: BOUNDARY CONDITIONS FOR CHARGED PERIODIC SYSTEMS

We first summarize the boundary conditions employed for Ewald summation and then discuss their relation to the Maxwell boundary conditions, which are the natural choice for our algorithm. The Ewald formula for the electrostatic energy of periodic a system is

$$U = \frac{1}{8\pi\epsilon_0} \sum_{i,j \neq i} e_i e_j \psi_{per}(\mathbf{r}_i - \mathbf{r}_j) + U_{self} + U_{dip} \quad (\text{A1})$$

The self-energy, $U_{self} = \kappa/\sqrt{\pi} \sum_i e_i^2$, is constant and therefore irrelevant for Monte-Carlo dynamics. The periodic Ewald potential ψ_{per} consists of sums in real and Fourier space:

$$\psi_{per} = \frac{4\pi}{L^3} \sum_{\mathbf{G} \neq 0} \frac{\exp(-G^2/4\kappa^2 + i\mathbf{G} \cdot \mathbf{r})}{G^2} - \frac{\pi}{\kappa^2 V} + \sum_{\mathbf{R}} \frac{\text{erfc}(\kappa|\mathbf{r} + \mathbf{R}|)}{|\mathbf{r} + \mathbf{R}|} \quad (\text{A2})$$

The result of the sum is independent of the range parameter, κ . At short distances, this expression can be expanded¹⁵, giving

$$\psi_{per} = const + \frac{1}{r} + \frac{2\pi r^2}{3L^3} + \mathcal{O}(r^4). \quad (\text{A3})$$

The second term is of the same order in $1/L$ as the dipole energy

$$U_{dip} = \frac{1}{2\epsilon_0(2\epsilon' + 1)L^3} \left| \sum_i e_i \mathbf{r}_i \right|^2. \quad (\text{A4})$$

This energy depends on the dielectric constant ϵ' of the surrounding medium. Two common choices for the dielectric constant are $\epsilon' = 1$ (‘‘vacuum’’) and $\epsilon' = \infty$ (‘‘tin foil’’).

A term comparable to U_{dip} arises when using Maxwell boundary conditions: In Sec. II, we saw that the field dynamics obey a Maxwell equation,

$$\frac{\partial \mathbf{E}}{\partial t} = -\mathbf{J}/\epsilon_0 + \text{curl } \mathbf{B}/\mu_0. \quad (\text{A5})$$

Integrating this equation over space and time, we find the relation between the $\mathbf{q} = 0$ component of the electric field and the dipole moment, \mathbf{d}

$$\bar{\mathbf{E}}(t) = -\frac{1}{L^3} \int dt \int d^3r \mathbf{J}/\epsilon_0 = -\mathbf{d}/L^3 \epsilon_0, \quad (\text{A6})$$

since the integral of the curl of a periodic function is zero. The contribution of $\bar{\mathbf{E}}$ to the electrostatic energy is

$$\mathcal{U}_d = \frac{\epsilon_0}{2} \int \bar{\mathbf{E}}^2 = \frac{\mathbf{d}^2}{2L^3\epsilon_0}, \quad (\text{A7})$$

The longitudinal components of \mathbf{E} for $\mathbf{q} \neq 0$ are given by the gradient of $\psi_{per}/4\pi\epsilon_0$.

Note that there is an important difference between the conventional dipole moment of the simulation cell, $\sum e_i \mathbf{r}_i$ and \mathbf{d} : A charge can wind about the periodic system giving equivalent configurations with different energies. These two definitions of the dipole moment are only the same modulo a Bravais lattice vector¹⁹:

$$\mathbf{d} = \sum_i e_i \mathbf{r}_i + |e|L\{l, m, n\}. \quad (\text{A8})$$

for arbitrary integers l, m, n .

Consider now a pair of particles with opposite charges separated by \mathbf{r} , simulated by our algorithm. If we sum over all equivalent configurations we find the relative statistical weight of a given state

$$\mathcal{Z}_0 = \sum_{l,m,n} e^{-e^2(\mathbf{r}+L\{l,m,n\})^2/2k_B T \epsilon_0 L^3}, \quad (\text{A9})$$

At low temperatures and with \mathbf{r} small the sum Eq. (A9) is dominated by a single minimum energy term with $l = m = n = 0$, thus

$$\mathcal{Z}_0 = e^{-e^2 \mathbf{r}^2 / 2k_B T \epsilon_0 L^3} \quad \text{for} \quad k_B T \ll e^2 / 4\epsilon_0 L \quad (\text{A10})$$

The corresponding free energy is

$$F = -kT \ln \mathcal{Z}_0 = e^2 \mathbf{r}^2 / 2\epsilon_0 L^3. \quad (\text{A11})$$

We now combine the low temperature result with the short distance expansion of the Ewald potential for two particles by adding Eq. (A11) to Eq. (A3). We find

$$V(r) = -e^2 \left(\frac{1}{4\pi\epsilon_0 r} + \frac{r^2}{6\epsilon_0 L^3} \right) + \frac{e^2 r^2}{2\epsilon_0 L^3}. \quad (\text{A12})$$

We thus expect a net quadratic correction $e^2 r^2 / 3\epsilon_0 L^3$ to the $1/r$ interaction as in Eq. (14).

In the opposite limit of high temperatures, the charges are mobile and the current can wind around the simulation cell many times. In this limit

$$\mathcal{Z}_0 \sim \text{const.} \quad \text{for} \quad k_B T \gg e^2 / 4\epsilon_0 L. \quad (\text{A13})$$

There are no dipole contributions in this limit, and the potential is that of Eq. (A3).

Note that the above arguments hold for free charges that allow the current to flow freely; for bound charges or dipoles the current does not lead to multiple inequivalent states for the field $\bar{\mathbf{E}}$. It is possible to impose the tinfoil boundary condition in our algorithm by introducing a third Monte-Carlo move that integrates over the total electric field $\bar{\mathbf{E}}$ (see also Ref. 10).

* Electronic address: joerg@turner.pct.espci.fr

† Electronic address: tony@turner.pct.espci.fr

¹ T. Schlick, R. D. Skeel, A. T. Brunger, L. V. Kalé, J. A. Board Jr., J. Hermans, and K. Schulten, *J. Comp. Phys.* **151**, 9 (1998).

² C. Sagui and T. Darden, *Annu. Rev. Biophys. Biomol. Struct.* **28**, 155 (1999).

³ J. W. Perram, H. G. Petersen, and S. W. de Leeuw, *Molecular Phys.* **65**, 875 (1988).

⁴ J. V. L. Beckers, C. P. Lowe, and S. W. de Leeuw, *Molecular Simulation* **20**, 269 (1988).

⁵ R. W. Hockney and J. W. Eastwood, *Computer Simulation using Particles* (Adam Hilger, 1988).

⁶ J. E. Barnes and P. Hut, *Nature* **324**, 446 (1986).

⁷ E. Essmann, L. Perera, M. L. Berkowitz, T. Darden, H. Lee, and L. G. Pedersen, *J. Chem. Phys.* **103**, 8577 (1995).

⁸ A. C. Maggs and V. Rossetto, *Phys. Rev. Lett.* **88**, 196402 (2002).

⁹ A. C. Maggs, *J. Chem. Phys.* **117**, 1975 (2002).

¹⁰ A. C. Maggs, e-print cond-mat/0304521 (2003).

¹¹ J. S. Schwinger, L. L. Deraad, K. A. Milton, and W. yang Tsai, *Classical Electrodynamics* (Perseus Books, 1998).

¹² C. Sagui and T. Darden, *J. Chem. Phys.* **114**, 6578 (2001).

¹³ S. W. de Leeuw, J. W. Perram, and E. R. Smith, *Proc. Royal Soc. London* **A373**, 26 (1980).

¹⁴ S. W. de Leeuw, J. W. Perram, and E. R. Smith, *Proc. Royal Soc. London* **A373**, 57 (1980).

¹⁵ L. M. Fraser, W. M. C. Foulkes, G. Rajagopal, R. J. Needs, S. Kenny, and A. J. Williamson, *Phys. Rev. B* **53**, 1814 (1996).

¹⁶ P. M. Chaikin and T. C. Lubensky, *Principles of condensed matter physics* (Cambridge University Press, 1995).

¹⁷ M. Deserno and C. Holm, *J. Chem. Phys.* **109**, 7678 (1998).

¹⁸ A. Pais, *Inward bound. Of matter and forces in the physical world.* (Oxford, 2002).

¹⁹ J.-M. Caillol, *J. Chem. Phys.* **101**, 6080 (1994).